Reionisation scenarios and the temperature of the IGM

Eric R. Tittley¹ and Avery Meiksin¹ *

¹SUPA†, Institute for Astronomy, University of Edinburgh, Blackford Hill, Edinburgh EH9 3HJ, UK

Accepted . Received ; in original form

ABSTRACT

We have explored reionisation of the universe using a radiative transfer (RT) code coupled to a particle-mesh (PM) N-body code. Multiple simulations were performed with different spectra of ionising radiation: a power law ($\propto \nu^{-0.5}$), miniquasar, starburst, and a time-varying spectrum that evolves from a starburst spectrum to a power law. The RT is sufficiently resolved in time and space to correctly model both the ionisation state and the temperature across the ionisation front. The temperature of the ionised intergalactic medium (IGM) is sensitive to the spectrum of the source of ionising radiation. The post-ionisation temperature is fairly insensitive to the redshift at which the hydrogen ionising sources turns on for expected scenarios. Hardening of the spectrum of the ionising radiation field due to passage through the high H_I column densities leads to fluctuations in the $f_{\rm He\,{\scriptscriptstyle II}}/f_{\rm H\,{\scriptscriptstyle I}}$ ratio in the shadowed regions. These variations alone, however, do not reproduce the measured fluctuations. The post-ionisation temperature of the IGM provides strong constraints on the nature of the sources of reionisation.

Key words: radiative transfer – cosmology: diffuse radiation – cosmology: large-scale structure of Universe – methods: numerical – methods: N-body simulations

1 INTRODUCTION

The process by which the Universe was reionised is one of the premier unsolved questions in cosmology. Measurements of the Ly α optical depth of the Intergalactic Medium (IGM) along Quasi-Stellar Object (QSO) lines-of-sight require the IGM to have been reionised by $z \gtrsim 6$ (Becker & et al 2001), consistent with recent measurements of the Cosmic Microwave Background (CMB) by the Wilkinson Microwave Anisotropy Probe (WMAP), although a higher redshift of $z \sim 11$ is preferred, with a 2- σ upper limit of $z \lesssim 17$ (Spergel & et al 2006). The sources of the reionisation are currently unknown. The most recent estimates of the numbers of high redshift QSOs suggest QSOs are too few to have ionised the H_I prior to $z \approx 4$, without an upturn in the QSO luminosity function at the faint end (Meiksin 2005). While an adequate supply of ionising photons is likely produced within young, star-forming galaxies, it has yet to be conclusively demonstrated that the ionising photons are able to escape in sufficient numbers to meet the requirements for reionisation (Fernández-Soto et al. 2003; Malkan et al. 2003). Other, more speculative, possibilities include pockets of Population III stars (e.g., in young galaxies or star clusters) or mini-quasars (Madau et al. 2004).

The post-reionisation IGM temperature may provide a

clue to the nature of the reionisation sources. Low density regions retain a memory of the post-reionisation temperature (Meiksin 1994; Miralda-Escude & Rees 1994). Evidence for temperatures in excess of the optically thin predictions at high redshifts (z>3) is provided by the widths of the low column density Ly α forest absorbers (Meiksin et al. 2001) which are expected to reside in the underdense regions comprising most of the volume of the universe (Zhang et al. 1998).

In the past few years, several groups have implemented numerical radiative transfer schemes for solving for the reionisation of the IGM (Abel et al. 1999; Gnedin & Abel 2001; Nakamoto et al. 2001; Razoumov et al. 2002; Ciardi et al. 2003; Whalen & Norman 2006). Most of the modelling of IGM reionisation has focused on the propagation of ionisation fronts (I-fronts), with less emphasis given to the postreionisation temperatures produced, as the required calculations are much more computationally demanding (Bolton et al. 2004).

Early estimates of the post-reionisation IGM temperature were made assuming optically thin gas. However, accounting for radiative transfer within the ionisation fronts leads to much higher temperatures.

In this paper, we use numerical simulations to assess the effect differing epochs of reionisation and source spectral shapes have on the post-reionisation temperature of the IGM. The simulations couple radiative transfer with an N-body code to model the evolution of the IGM.

 $^{^\}star$ E-mail: ert@roe.ac.uk (ERT); aam@roe.ac.uk (AM)

[†] Scottish Universities Physics Alliance

Table 1. Identifiers for the various models used in this paper.

Model	8	$z_{ m on}$ 12	20
Power Law	PL08	PL12	PL20
Mini-quasar	MQ08	MQ12	MQ20
Star burst	SB08	SB12	SB20
Hybrid	HY08	HY12	HY20

2 SIMULATIONS

The passage of an ionisation from from various sources through a volume of intergalactic medium (IGM) was simulated numerically. For each source, a different numerical simulation was performed. The sources were varied by their spectrum and their "turn-on" redshift, as summarised in Table 1. In §2, the numerical code, the simulation volume, and the sources are described in greater detail. Results of the simulations are provided in §3 and discussed in §4.

2.1 Method

The simulation code, PMRT.mpi, is the combination of a Lagrangian particle-mesh (PM) code and a grid-based radiative transfer (RT) code which are modularly independent. The PM code (Meiksin et al. 1999) evolves the density field assuming all mass is collisionless, interacting only gravitationally. The gas density is taken as a constant fraction (Ω_b/Ω_m) of the total density. The RT code uses a probabilistic method which is based on the photon-conserving algorithm of Abel et al. (1999) extended to include helium by Bolton et al. (2004). Previously Bolton et al. (2004) applied the RT algorithm to a density field frozen in the comoving frame. In our implementation, we apply the algorithm to an evolving density field, as computed by the PM code.

In addition to providing accurate positioning of the ionisation front, special attention is given to computing accurate post-photoionisation temperatures. This requires sufficient resolution in time and space to correctly model both the ionisation structure of the ionisation front and the temperature across it. This is particularly important when modelling reionisation by sources with hard photons like QSOs.

Of course, the effort required to get the temperatures correct comes at the expense of CPU cycles. More than 20000 CPU hours were required for the simulations presented here. PMRT_mpi was run in parallel on 8 or 16 CPUs drawn from a dedicated cluster of IBM OpenPower 720s or a local cluster of Linux boxes of mixed type.

Both the PM and RT modules are coded in C and parallelised using a message passing interface (MPI). MPI is suited to work on distributed memory systems, but works equally well on shared memory systems, albeit not with optimal memory use. The RT module consumes most of the processing time. In the RT module, each line of sight (LOS) is processed by a single CPU. In general the time spent by each process on a LOS scales linearly with the resolution along the LOS, although the number of refinements is a factor. Load imbalance is possible because the time to process a LOS varies for each LOS, depending on the amount of structure. Load imbalance is alleviated by dynamic (first-

come-first-serve) allocation of LOSs to processes. The master node performs the allocation and, consequently, has a significantly lower mean load. The load imbalance with the master node can be reduced by either 1) having one physical processor unit execute both the master and a slave process or 2) using many processor units, so that instead of one-of-few being underused, one-of-many is underused and less time is spent in a non-load-balanced state.

The ionising radiation is projected as parallel rays normal to the surface of the volume. This configuration has the computational advantage of allowing all radiative calculations for a given ray to be done in a single column, independent of neighbouring columns. Since no information about the thermal state of the gas is carried with the particles as they moves from one cell to another, each column can be interpreted as an individual line of sight which is independent of any other line of sight.

In addition to not including advection of ionisationstate parameters across cells, the simulations are limited in not solving for the overlapping of ionisation fronts in the current implementation. Rather, they describe the passing of the first ionisation front across a neutral region. Also, the simulations do not include diffuse radiation. In general, radiative recombinations produce a diffuse field throughout the ionised region, although the intensity depends on the amount of clumping of the gas. Estimates for the boost in the ionisation rate range from 10 per cent to 40 per cent. (Meiksin & Madau 1993; Haardt & Madau 1996).

We select 256 lines of sight arranged in a plane to assist in visually interpreting the passage of the front while providing enough lines of sight to deal with cosmic variance.

2.2 Simulation Volume

All simulations were performed in a $(25h^{-1} \,\mathrm{Mpc})^3$ comoving volume. The concordance $\Lambda\mathrm{CDM}$ model was assumed (Spergel et al. 2003), with parameters: h = 0.71, $\Omega_b h^2 = 0.022$, $\Omega_m = 0.268$, $\Omega_v = 0.732$, where h, Ω_b , Ω_m , and Ω_v have their usual meanings as the Hubble parameter ($H_0 = 100h\,\mathrm{km\ s^{-1}\ Mpc^{-1}}$, where H_0 is the present day value of the Hubble parameter), and the contributions to Ω from the gas, all matter, and the vacuum energy, respectively.

The initial density perturbations were created by displacing a uniform grid using the Zel'dovich approximation. The initial power spectrum of the density fields was a COBE-normalised power law with index n=0.97. The same initial conditions were used for all simulations, except for the convergence tests. Since there is no feedback from the RT to the PM code, all the runs have identical gas densities.

The simulations were evolved to a redshift of 3 by which point we know both hydrogen and helium in the universe were completely ionised.

2.3 Sources

The source spectra (Fig. 1) were selected to emulate candidate reionisation sources. For the power law, the luminosity is given by $L(\nu) \propto \nu^{-\alpha}$ where $\alpha = 0.5$, which corresponds to a hard quasar/QSO/AGN spectrum. The mini-quasar spectrum of Madau et al. (2004) is given by $L(x) \propto x^{1/4} + 8x^{-1}$,

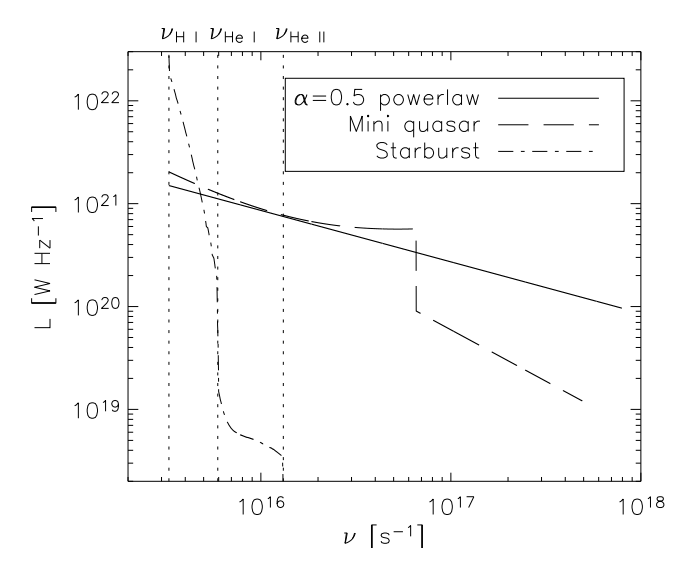


Figure 1. Source spectra. The ionisation thresholds for H I, He I, and He II are indicated.

 $1 \le x \le 20$; $P(x) \propto 8x^{-1}$, $x \ge 20$ where $x \equiv \nu/\nu_0$. The starburst spectrum was produced by PÉGASE¹ (Fioc & Rocca-Volmerange 1997) for a galaxy 30 Myr after a burst of Pop III (zero metallicity) star formation. The starburst spectrum has an effective spectral index of $\alpha_{\rm eff} = 7.4$ just above the Lyman edge. The hybrid model begins with a starburst spectrum, and between z=5 and z=4 evolves into an $\alpha=0.5$ power law.

The order of propagation of the He I and He II ionisation fronts is different in the different models. For a time-invariant spectrum, the He II I-front precedes the H I I-front if the spectrum is hard enough, specifically if $\alpha_{\rm eff} < 1.8$. The condition is met for both the power law and miniquasar spectra and, indeed, the He II was ionised prior to H I in those simulations. The starburst spectrum certainly fails the condition as it has negligible intensity above $\nu_{\rm He II}$. The hybrid spectrum, in which a spectrum dominated by starbursts evolves into one dominated by a power law, leads to the H I I-front preceding that of He II.

All spectra were normalised to produce ionising photons at the rate of $1.5 \times 10^7 (1+z)^2 \, \mathrm{s}^{-1} \, \mathrm{m}^{-2} \, (L[\nu_{\mathrm{H\,I}}] = 1.5 \times 10^{21} \, \mathrm{W} \, \mathrm{Hz}^{-1}$ for an $\alpha = 0.5$ power law source at a comoving distance of 5 Mpc). The flux is sufficient for the ionisation front to cross the volume by z = 3.

To explore the effect of reionisation redshift, for each source we performed simulations with the source turning on at redshifts of $z_{\rm on}=8,\,12,$ and 20. These were selected to cover the range of redshifts limited by the WMAP and QSO observations.

Each source was located outside the volume 5 comoving Mpc from the edge. Half the Strömgren radius for the mean physical density at the redshift the source turned on in a non-expanding universe is 4, 6, and 8 comoving Mpc for $z_{\rm on}=20,12,$ and 8, respectively. The volume between the source and the edge of the volume was assumed to be a vacuum, which is a good approximation to the low-opacity, highly ionised state it would have so close to the source.

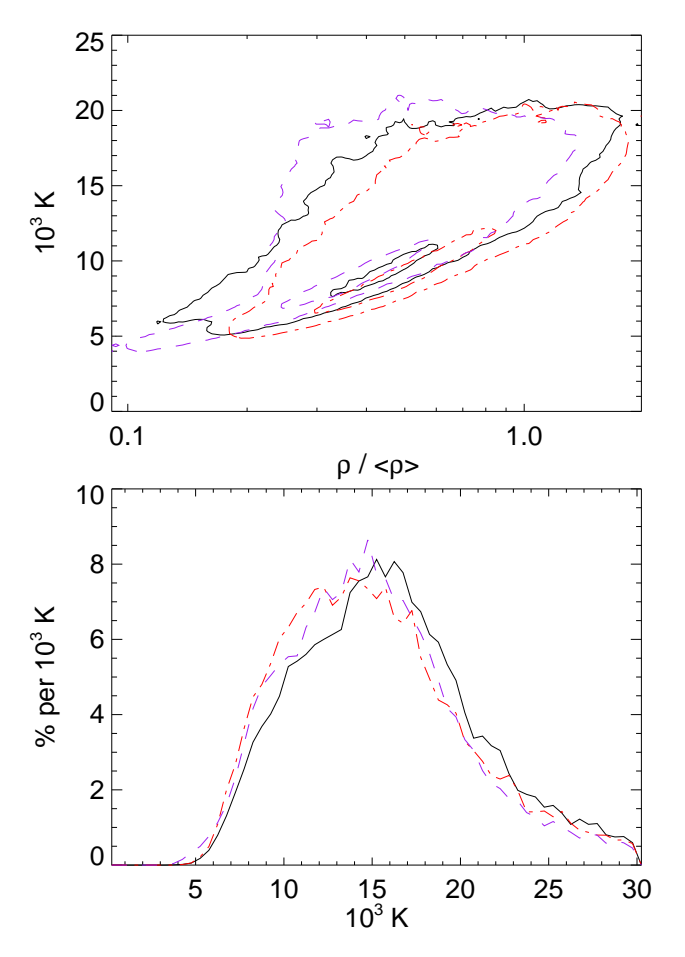


Figure 2. Convergence with resolution of the N-body code and the effect of cosmic variance. The top panel illustrates the $\rho-T$ distribution for the ionised gas for two $N_p=256^3$, $N_g=256$ realisations with the same power law model (black/solid and red/dashdot) and a $N_p=512^3$, $N_g=512$ realisation (purple/dashed). The contour intervals are spaced by a factor of 10. The bottom panel shows the mass-weighted temperature distributions for the ionised gas for the same models.

The radiation field takes the plane-wave approximation and is not attenuated by r^{-2} . A limited number of simulations performed with the radiation field attenuated by r^{-2} produced results similar to those without the attenuation.

For brevity, the labels listed in Table 1 will be used henceforth to identify the various simulations with their combination of model spectrum and source turn-on redshift.

2.4 Cosmic variance, convergence

The results are subject to cosmic variance and bias from the resolution of the N-body code and the RT grid, but not substantially. In this section we describe two extra simulations which ascertain the effects of cosmic variance and a change in the resolution parameters by comparing these with the PL08 run which they most closely match. We use the $\rho-T$ and temperature distributions (Fig. 2 top and bottom panels.) to illustrate the effects.

There are two parameters that control the spatial resolution of the simulation: the number of particles in the PM simulation, N_p , and the mesh size of the gas density grid,

http://www2.iap.fr/users/fioc/PEGASE.html

4 Eric R. Tittley and Avery Meiksin

 N_g . To estimate the variation due simply to cosmic variance, a simulation was run with a different realisation of the initial density fluctuations at the same resolution as the main body of runs ($N_p=256^3$, $N_g=256$). In Fig. 2, the difference between the solid (black) and dot-dashed lines (red) indicates the cosmic variance. A simulation with 8 times the mass resolution ($N_p=512^3$) and twice the RT mesh resolution ($N_g=512$) produced a qualitatively equivalent distribution (Fig. 2, dashed line), bracketed by the two lower resolution realisations.

3 SIMULATION RESULTS

The simulations provide information for two epochs of interest: the period during which the gas is being ionised and the post-ionisation epoch. Our primary focus in this paper is the post-ionisation state of the gas, but future telescopes such as the Low Frequency Array 2 (LOFAR), the Mileura Widefield Array 3 (MWA), and eventually the Square Kilometre Array 4 (SKA), will be able to probe the epoch of ionisation itself via the red shifted 21cm line of neutral hydrogen. The re-ionisation phase will be the topic of a future paper.

Our principal goal for this study is to determine if the temperature of the ionised IGM is dependent on the nature of the ionising source and the redshift at which ionisation commenced. The answers are, respectively, "yes" and "no". In Sec. 3.1 we quantify and discuss these answers.

Further understanding of the state of the IGM is provided by the ionisation rates which set the relative abundances of species. The rates in our simulations are described and discussed in Sec. 3.2.

Because of the inclusion of helium ionisation in our simulations, we are able to produce information concerning the ratio of He II and He III to H I in the ionised IGM. We discuss these results in Sec. 3.3.

Clumping of the gas impedes the propagation of ionisation fronts. We evaluate the importance of the effect in Sec. 3.4

By z=3 we know the hydrogen in the IGM was fully ionised. This of course does not mean there is no H_I. For purposes of discussion in this paper, we will consider the gas ionised if the ionisation fraction $f_{\rm H{\sc i}}<0.1$. Figure 3 maps $f_{\rm H{\sc i}}$ in the simulation volumes. Our criterion is met only in the areas mapped grey to white. In all simulations, hydrogen is ionised throughout the bulk of the volume by z=3.

The importance of including radiative transfer effects during reionisation to obtain accurate temperatures is best illustrated by comparing against a simulation using the optically thin approximation (OTA). Simply put, the OTA means all points not near a source receive the same average radiation field. The approximation works fairly well because any gas dense enough to self-shield is also dense enough to reach thermal balance. So the post-reionisation temperature is essentially insensitive to the details of reionisation. The approximation fails, however, to properly treat low density gas, because the time to reach thermal equilibrium in low

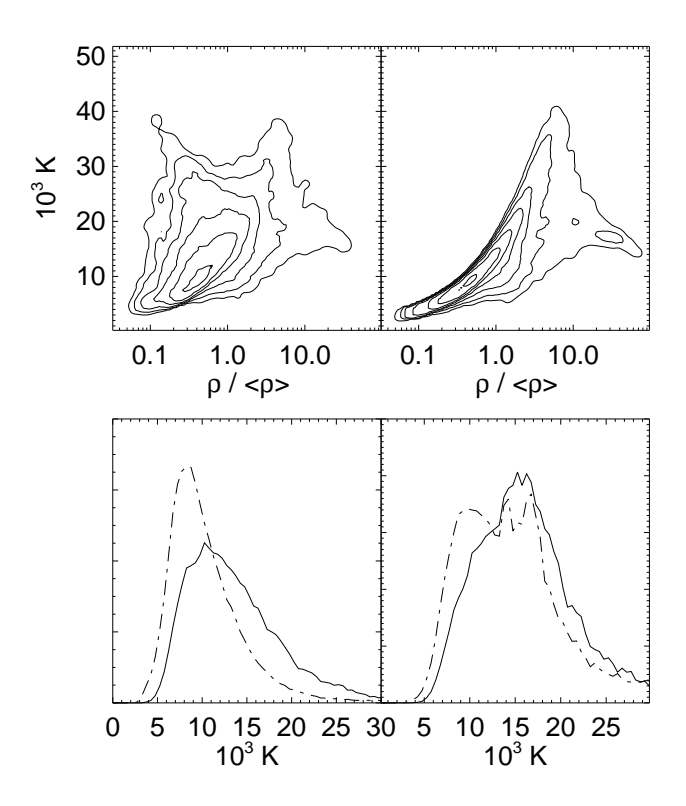


Figure 4. Effects of optically thin approximation. The top panels illustrate the $\rho-T$ distribution without (left) and using (right) the optically thin approximation. The lower panels show the modification to the volume-weighted (left) and mass-weighted (right) temperature distributions produced without (solid) and with (dot-dashed) the approximation.

density gas exceeds the Hubble time at high redshifts. As a consequence, the low density gas retains a memory of the reionisation details. This is particularly important when low density gas is shielded from the oncoming I-front by dense structures because of their role in hardening the spectrum of the radiation field.

3.1 Temperature

To compare our results with those using the OTA, we performed a simulation in which the cumulative optical depth to any point was set to zero, mimicking the OTA. The $\rho-T$ and temperature distributions for the PL08 model with and without the approximation are illustrated in Fig. 4. Overall the distributions are similar. Since different regions are exposed to different spectra without the OTA, there is more spread than when the OTA is used. The hardening of the spectrum due to selective absorption of low-energy photons heats the gas, particularly in the less dense regions. A high density spur of decreasing temperature with increasing density is produced in both simulations, resulting from the establishment of thermal balance between photoionisation heating and atomic cooling (Meiksin 1994).

Figure 5 is a map of the temperature distribution at a redshift of z=3. We immediately see a variety of effects that will be explored quantitatively later. First, the gas temperature in the mini-quasar model is virtually identical to that of the simple $\alpha=0.5$ power law. Second, the star-burst

 $^{^2}$ www.lofar.org

 $^{^3}$ web.haystack.mit.edu/arrays/MWA/site/index.html

⁴ www.skatelescope.org

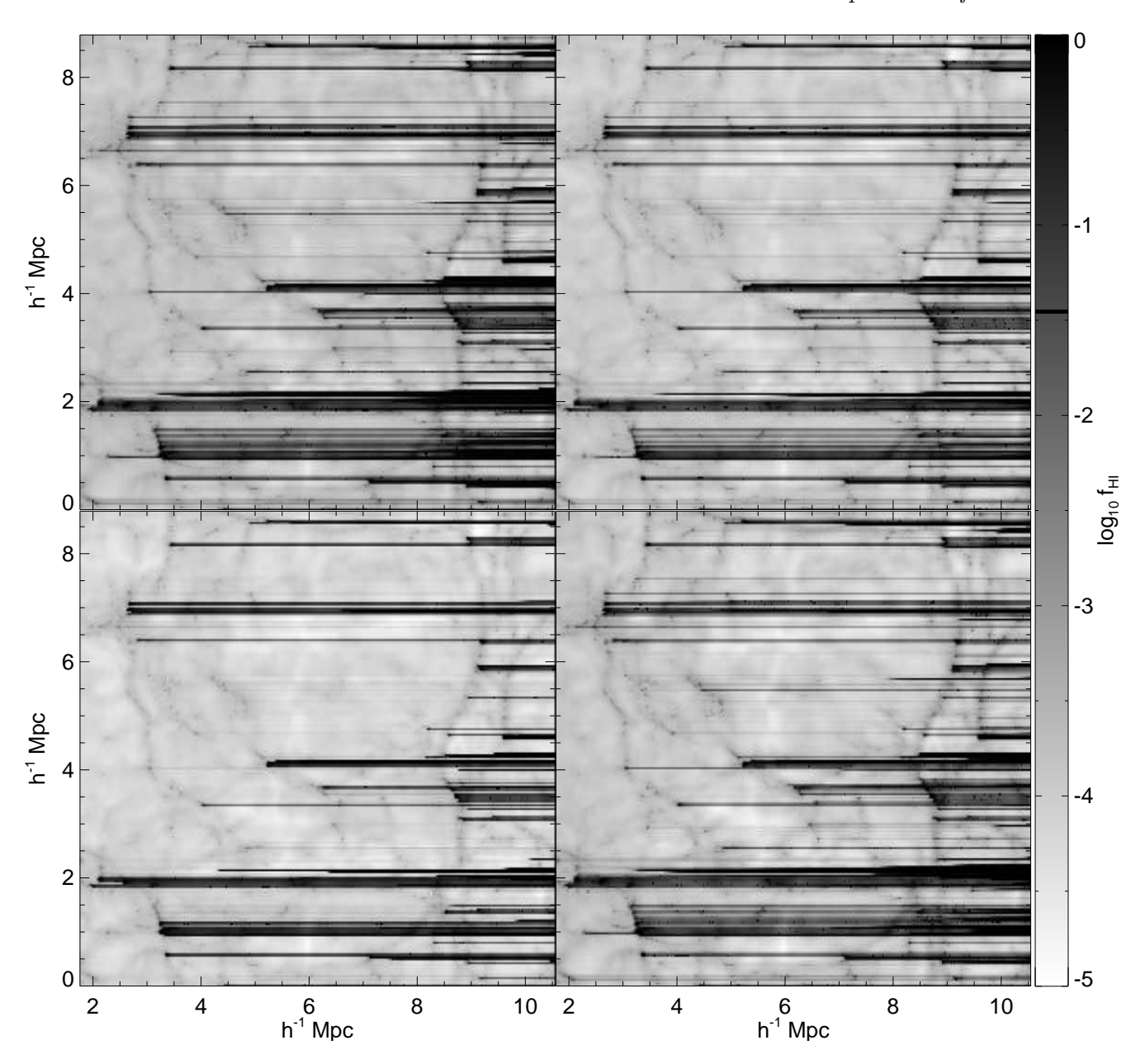


Figure 3. The H I fraction at z=3. From top-left to bottom-right the panels correspond to PL20, MQ20, SB20, and HY20.

model produces the coolest ionised gas. Third, the highest temperatures are generated by the hybrid model. Fourth, a "shadow" effect is apparent, particularly for the hybrid model. Unsurprisingly, gas in the shadows cast by knots of gas is cooler than the ambient temperature. However, when the HeII front works through the knot, the previously shadowed gas is heated above the ambient temperature. Finally, when compared with the gas density, all the models produce gas temperatures with structure that traces the large-scale structure, as demonstrated in Fig. 6. The relation, however, is not one of simple proportionality, as we will see below. For instance, because the most recently ionised gas tends to be hotter at a given density, the temperature tends to increase towards the right (because the I-front passes from left to right), as shown in Fig. 5.

The final gas temperatures distinguish the various mod-

els. The temperature distributions of the ionised gas both volume-weighted (Fig. 7) and mass-weighted (Fig. 8) show clear differences based on the models. For the power-law and mini-quasar models, the temperatures span 8 to $30\times 10^3~\rm K$ (90 per cent of the gas with 5 per cent below the range and 5 per cent above) with a mean of $17\times 10^3~\rm K$ (mass-weighted). The hybrid model has a hotter tail in its distribution, ranging from ~ 11 to $34\times 10^3~\rm K$ with a mean of $20\times 10^3~\rm K$. Gas three times cooler is produced by the star-burst model. For this model, the temperatures range from 2000 to 18000 K with the mean at $6600~\rm K$, though the distribution is highly skewed with the mode at $3000~\rm K$.

The redshift at which the source turns on is not a significant factor. In both Fig. 7 and Fig. 8, the turn-on redshifts of the models are distinguished in the temperature distributions by the line type. Save for a slight shift to higher

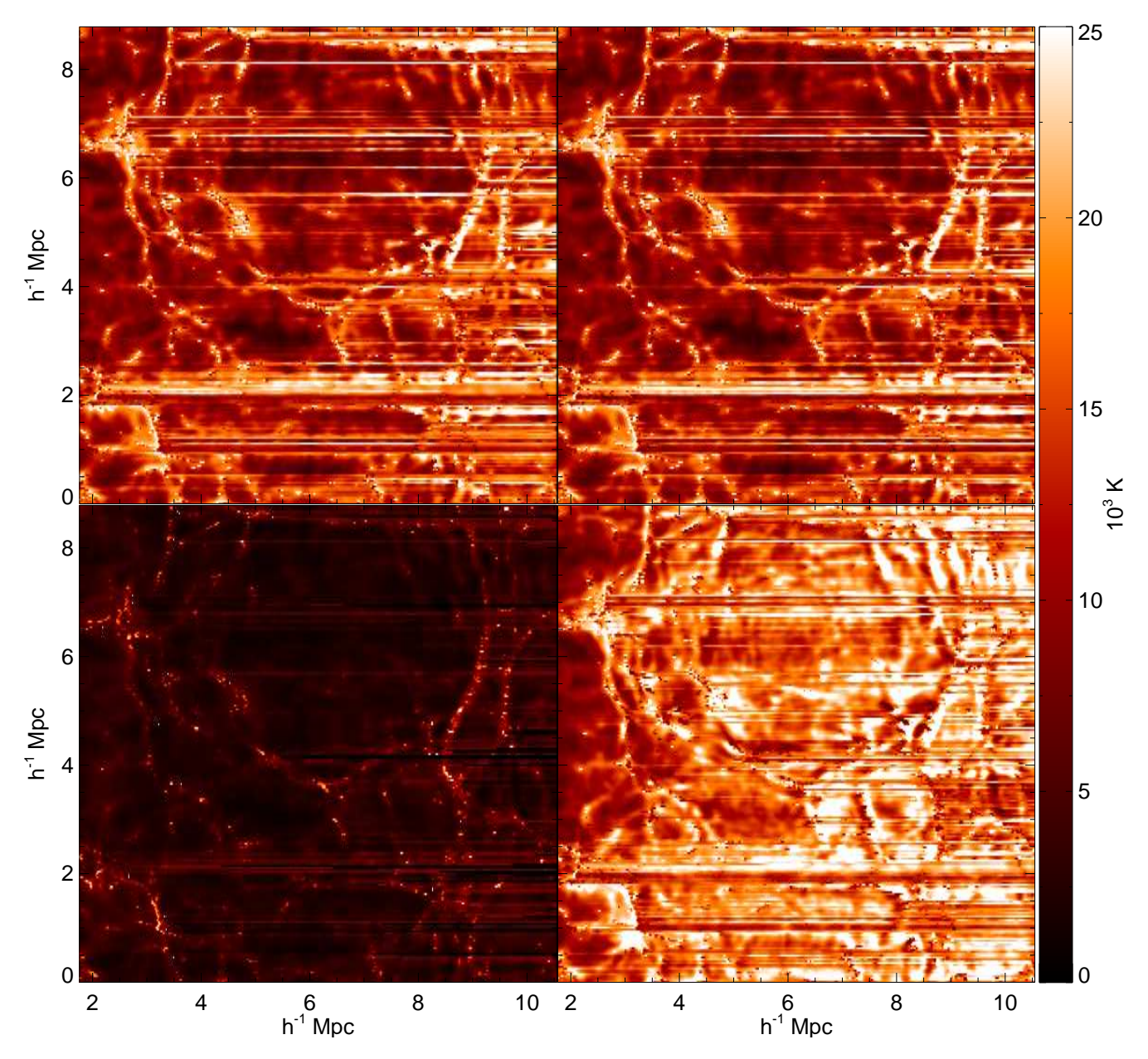


Figure 5. The temperature at z = 3. From top-left to bottom-right the panels correspond to PL20, MQ20, SB20, and HY20. The source is to the left. Cool (dark) streaks are shadowed regions. Hot streaks are regions recently unshadowed.

temperatures for the $z_{\rm on}=8$ models, the curves are nearly identical.

As we showed above, the use of full radiative transfer instead of an optically thin approximation not only further heats the gas, but it spreads the $\rho-T$ distribution away from a tight power law (Fig. 4). The spread in temperatures is greatest for gas with $\rho/\bar{\rho}<1$. The spectrum of the ionising radiation is modified by preferential absorption of the low frequency component as it passes through the gas. The modification hardens any spectrum, but is most influential to spectra that already have a hard component. Hence, the spread should be largest for harder spectra. Figure 9, which maps the $\rho-T$ distribution at z=3 for the ionised gas for PL20, MQ20, SB20, and HY20, confirms the larger spread in the harder spectra. Also confirmed is the similarity of

the state of the gas in the models with the power law and miniquasar spectra.

We fit a polytropic relation, $T=T_0(\rho/\bar{\rho})^{\gamma-1}$, to the $\rho-T$ distributions, and find $T_0=15000\pm200$, 14800 ± 200 , 3700 ± 50 , 19300 ± 200 and $\gamma=1.52\pm0.01$, 1.53 ± 0.01 , 1.54 ± 0.01 , 1.13 ± 0.01 for the PL20, MQ20, SB20, and HY20, respectively, at z=3. Note the errors are for the coefficients and not an indication of the spread of the $\rho-T$ distribution, which is not particularly well-described as a single polytropic dependence. For comparison, for the OTA run, for which local heating is balanced by local cooling, we find $T_0=13780\pm40$ and $\gamma=1.527\pm0.003$. Together, these very different simulations imply a local balance between heating and cooling still dominates the setting of the polytropic index. The exception is the value of γ for the

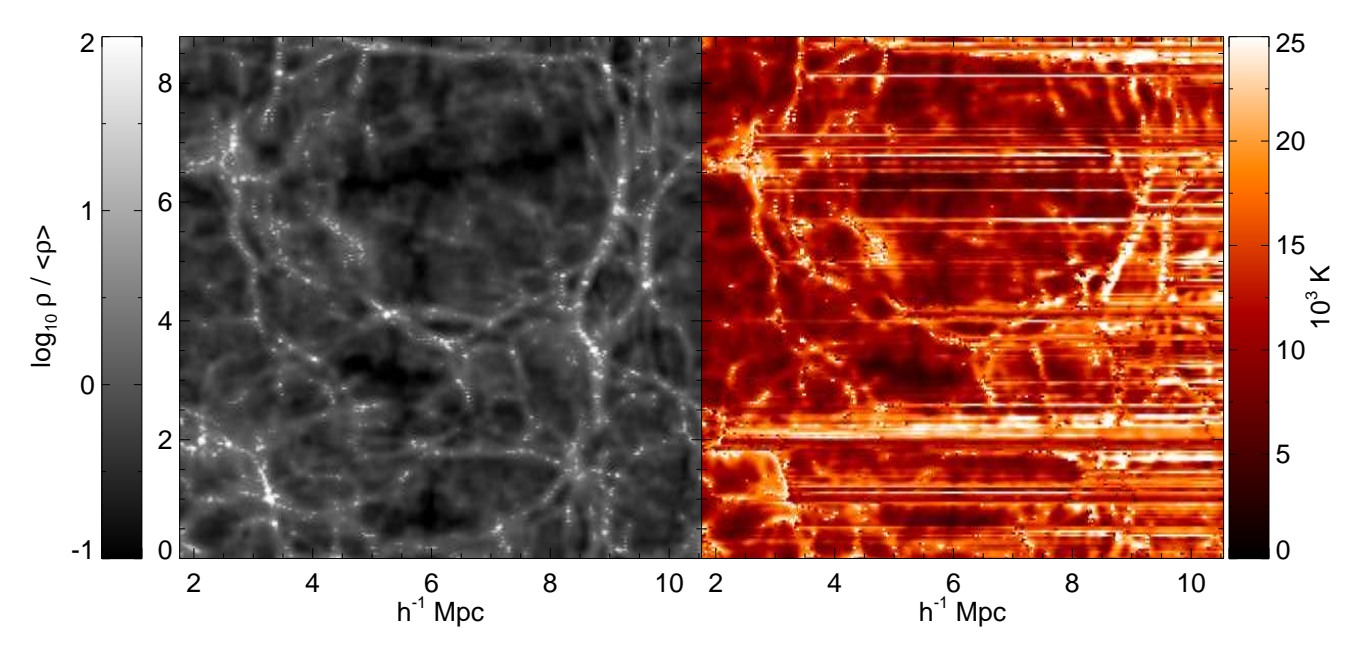


Figure 6. Density distribution and temperature map. The temperature map is from PL20. Both maps are for z=3.

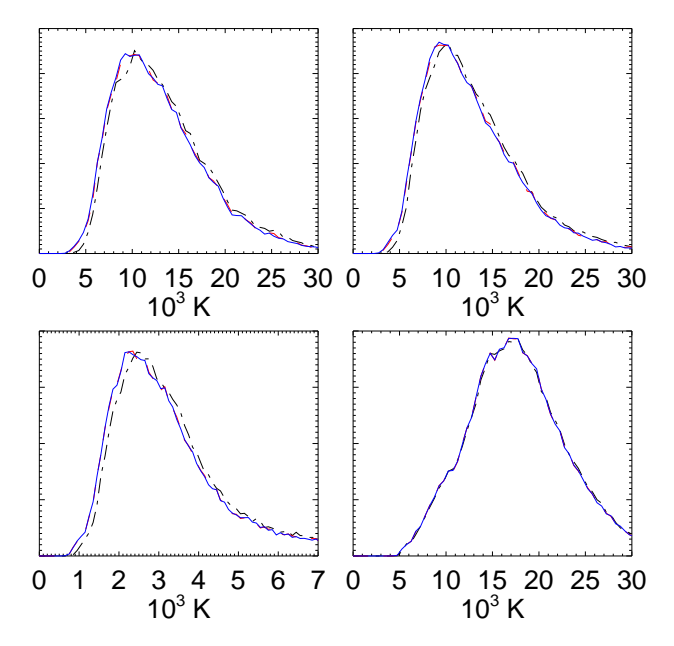


Figure 7. The volume-weighted temperature distribution at z=3 for the ionised gas only. From top-left to bottom-right the panels correspond to the power law, mini-quasar, star burst, and hybrid model. The colours distinguish the redshift at which the source turns on, with $z_{\rm on}=8$ black/dash-dot, $z_{\rm on}=12$ red/dashed, and $z_{\rm on}=20$ blue/solid. The dashed and solid lines nearly coincide. Note the change in the temperature scale.

hybrid model, for which entropy is injected at all densities. For all models, the index is lower than the adiabatic index, $\gamma_{\rm ad}=5/3$, reflecting the influence of radiative cooling in high-density regions.

These results may be compared with the polytropic fits of Schaye et al. (2000) to Keck HIRES spectra. These authors find $T_0 \approx 2.2 \pm 0.2 \times 10^4$ K and $\gamma \approx 1.0 \pm 0.1$ at $z \approx 3$,

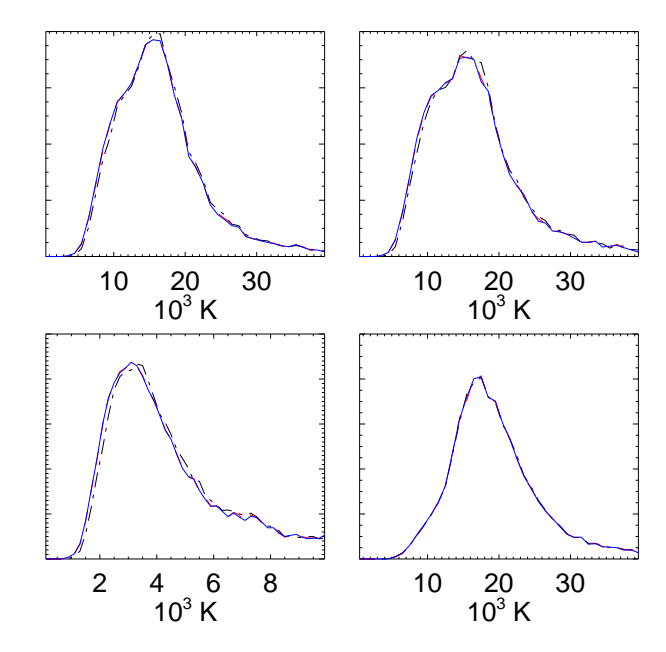


Figure 8. The mass-weighted temperature distribution at z=3 for the ionised gas only. From top-left to bottom-right the panels correspond to the power law, mini-quasar, star burst, and hybrid model. The line types distinguish the redshift at which the source turns on, with $z_{\rm on}=8$ black/dash-dot, $z_{\rm on}=12$ red/dashed, and $z_{\rm on}=20$ blue/solid. The dashed and solid lines nearly coincide.

values most consistent with the late $\mbox{He\,{\sc ii}}$ reionisation hybrid model.

3.2 Ionisation Rates

The varying optical depth to ionising photons results in fluctuations in the ionising background. The ionisation background is parametrized by the ionisation rate, /Gamma, which is the number of photoionisations per atom per unit

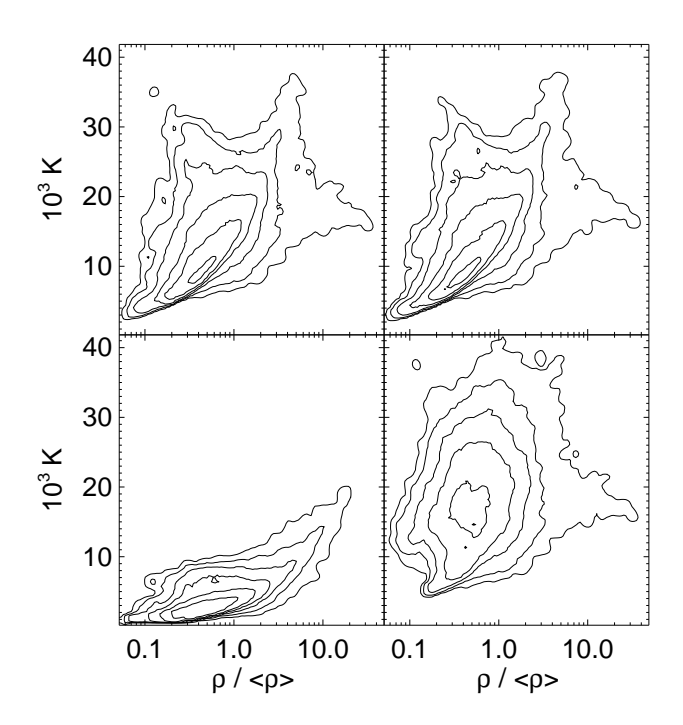


Figure 9. The $\rho-T$ distribution at z=3 for the ionised gas only. From top-left to bottom-right the panels correspond to PL20, MQ20, SB20, and HY20. The contour intervals are spaced by a factor of $\sqrt{10}$.

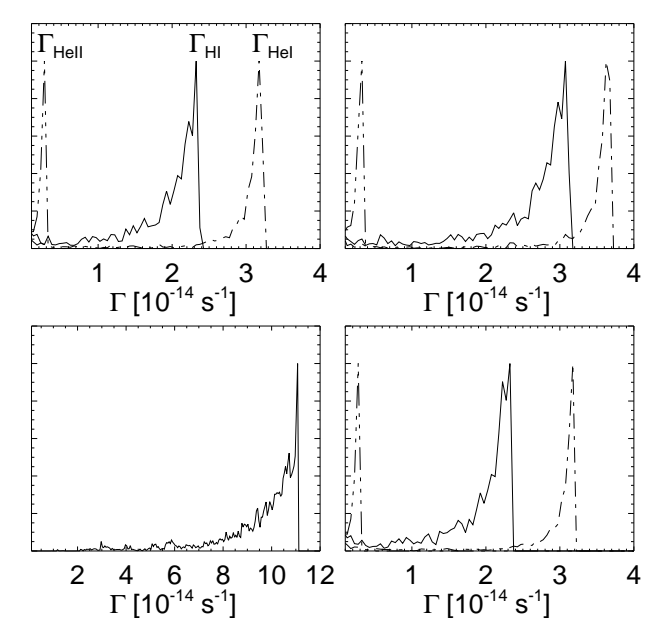


Figure 10. Distribution functions for the ionisation rates at z=3. From top-left to bottom-right the panels correspond to power law, miniquasar, starburst, and hybrid models. The redshift at which the source turns on is indistinguishable. Only rates for the hydrogen-ionised gas are plotted. The total ionisation rate is given by the solid line. The contributions from the various species are distinguished as indicated. The only contribution to the starburst distribution comes from hydrogen. Note the different Γ range for the starburst model.

time. A long tail towards low ionisation rates is found, as shown in Fig. 10. The sharp cut-off at the high end corresponds to low optical depth to the source leading to negligible filtering of the source spectrum. Any filtering hardens the spectrum and lowers Γ . A tail is similarly found in the simulations of Maselli & Ferrara (2005), although without the sharp cut-off at the high end. They model a uniform radiation field and use the optically thin approximation. For an optically thin approximation (see Sec. 3.1), Γ_i for species i has a single value at the location of the upper edge of the Γ_i distribution in Fig. 10. The absence of the cut-off in the simulations of Maselli & Ferrara (2005) is consistent with the discreteness effects of their Monte Carlo radiative transfer approach. Note that without the plane-wave approximation in our simulations, the upper edge would have a r^{-2} dependence, so distributions like those seen in Fig. 10 would be found only for constant r. Indeed, Meiksin & White (2003) show that in the presence of local randomly distributed ionisation sources, the sharp cut-off would be replaced by a power-law tail varying as $\Gamma_{\rm HI}^{-2.5}$.

3.3 Helium

Helium provides a further diagnostic of the conditions in the IGM. By having two ionisation states, both at higher energy than that of H_I, helium provides information about the abundance of high-energy photons. The ratio of the hydrogen and helium column densities is consequently a function of the spectral shape of the ionising radiation. Coinciding H_I and He_{II} absorption features in QSO spectra have been compared by Zheng et al. (2004) and Reimers et al. (2005). These observations place constraints on the ionisation state and temperature of the gas, which in turn constrain the reionisation models. As an additional source of heating, helium photoionisation will also boost the temperature of the gas.

If there is sufficient flux at $\nu > \nu_{\rm He\,II}$, the helium is ionised almost entirely to He III before the hydrogen becomes ionised. This case leads to two domains: 1) $f_{\rm H\,I} \sim 1$ and $f_{\rm He\,III} \sim 0$ to 1, and 2) $f_{\rm He\,III} \sim 1$ and $f_{\rm H\,I} \sim 0$ to 1. Singly ionised helium, He II, follows a more complicated history. In the presence of a hard spectrum He II is created prior to hydrogen ionisation, then destroyed concurrently with neutral hydrogen. This produces the sickle-like $f_{\rm H\,I} - f_{\rm He\,II}$ relation illustrated in Fig. 11. The sharpness of the cusp at large $f_{\rm H\,I}$ and $f_{\rm He\,II}$ is set by the amount of He II destruction prior to hydrogen ionisation.

The hydrogen and helium ionisation states are highly correlated when the source ionises He II. In the form $f_{\rm He \, II} = \alpha f_{\rm HI}^{\beta}$, $\alpha = 48.81 \pm 0.07$, 59.88 ± 0.07 , 41.92 ± 0.05 and $\beta = 1.0153 \pm 0.0002$, 1.0204 ± 0.0001 , 0.9966 ± 0.0001 for PL20, MQ20, and HY20 respectively. We estimated the errors using a bootstrap method. The errors are to the fit and do not indicate the distribution about the fit nor include cosmic variance. We used the two PL08 runs with different initial conditions to estimate the degree to which cosmic variance affects the results. For $f_{\rm He \, II} = \alpha f_{\rm HI}^{\beta}$, α varies by 0.2 per cent. and β by 0.02 per cent. Clearly $f_{\rm HI}$ and $f_{\rm He \, II}$ are linearly related.

The ionisation states of hydrogen and helium are expected to be linearly correlated but dependent on the hard-

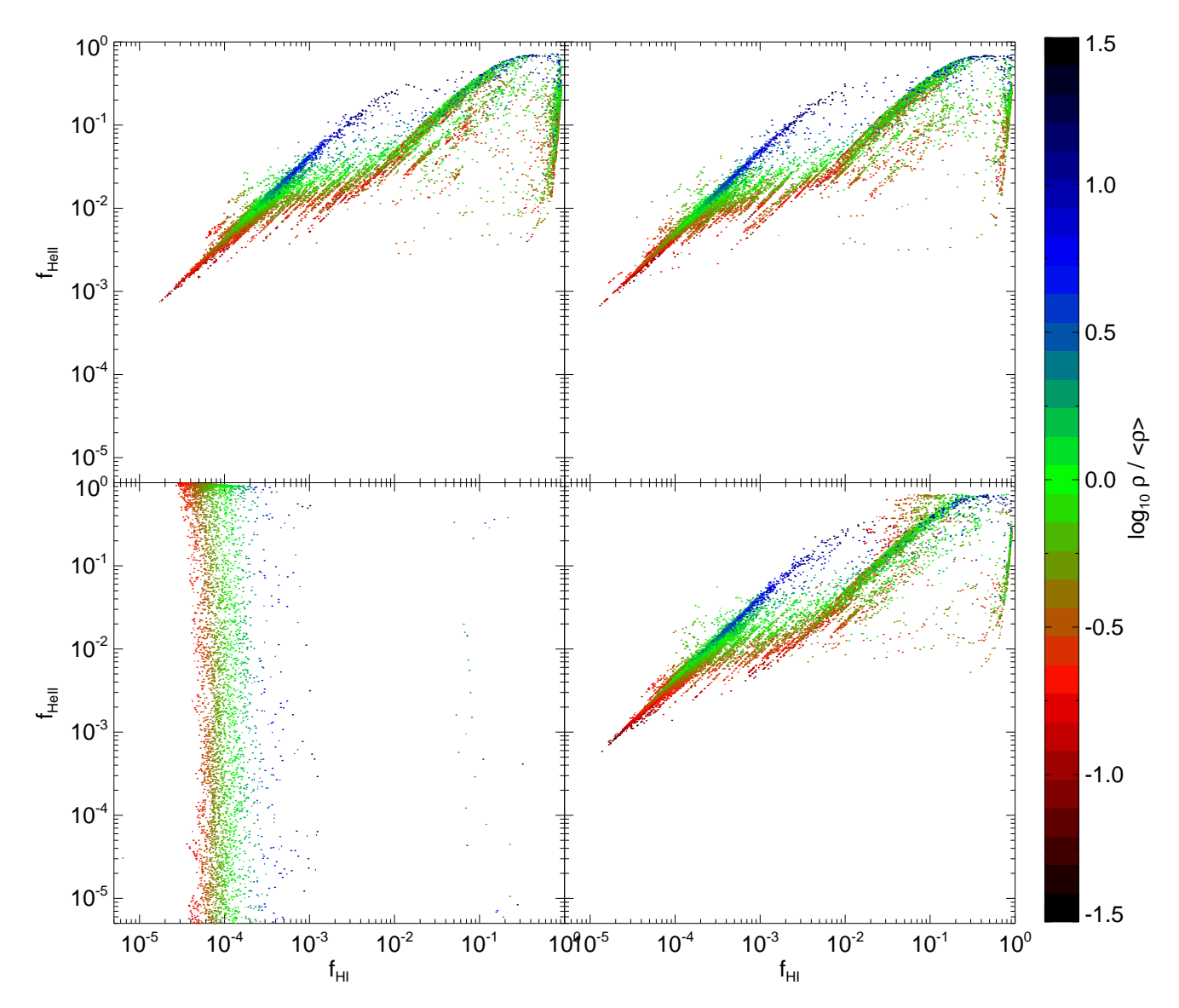


Figure 11. HeII versus HI fractions showing dependency on density at z = 3. From top-left to bottom-right the panels correspond to PL20, MQ20, SB20, and HY20.

ness of the local radiation field. In radiative equilibrium, the rate equations for hydrogen and ${\rm He\,{\sc ii}}$ are

$$n_{\rm H\,{\scriptscriptstyle I}}\Gamma_{\rm H\,{\scriptscriptstyle I}} = n_e n_{\rm H\,{\scriptscriptstyle I}{\scriptscriptstyle I}}\alpha_{\rm H\,{\scriptscriptstyle I}{\scriptscriptstyle I}}$$

$$n_{\mathrm{He\,II}}\Gamma_{\mathrm{He\,II}} = n_e n_{\mathrm{He\,III}} \alpha_{\mathrm{He\,III}} + n_{\mathrm{He\,I}}\Gamma_{\mathrm{He\,I}}$$

where, for species i, n_i is the number density, Γ_i is the number of photoionisations per atom per unit time, and α_i is the recombination coefficient. For the highly ionised gas in the simulations, $f_{\rm H\,\tiny I}\Gamma_{\rm H\,\tiny I} \simeq n_e\alpha_{\rm H\,\tiny II}$ and $f_{\rm He\,\tiny II}\Gamma_{\rm He\,\tiny II} \simeq n_e\alpha_{\rm He\,\tiny III}$ giving

$$\frac{f_{\rm He\,II}}{f_{\rm H\,I}} \simeq \frac{\alpha_{\rm He\,III}}{\alpha_{\rm H\,II}} \frac{\Gamma_{\rm H\,I}}{\Gamma_{\rm He\,II}}.\tag{1}$$

Since HeII is a hydrogen-like species, the recombination coefficients scale similarly with temperature. Over the range 10,000 K to 20,000 K, $\alpha_{\rm He\,III} \simeq 5.3\alpha_{\rm H\,II}$. Similarly, the photoionisation rates also scale but in a more complicated manner dependent on the spectrum. The photoionsation rate is

dependent on the local mean intensity of radiation, J_{ν} , and the ionisation cross section for species i, a_i , by

$$\Gamma_i = 4\pi \int_{\nu_0}^{\infty} \frac{J_{\nu}}{h\nu} a_i d\nu. \tag{2}$$

The cross sections for H_{1} and H_{2} can be approximated by (Osterbrock 1989)

$$a_i(\nu) = \sigma_i \left[\beta_0 \quad \frac{\nu}{\nu_i} \quad ^{-s_0} + (1 - \beta_0) \quad \frac{\nu}{\nu_i} \quad ^{-s_0 - 1} \right]$$
 (3)

with β_0 and s_0 the same for hydrogen-like species and $\sigma_{\rm He\,II} = \sigma_{\rm H\,I}/4$ and $\nu_{\rm He\,II} = 4\nu_{\rm H\,I}$. Taking the radiation field to have the form $J_{\nu} \propto \nu^{-\alpha}$, the integral in Eq. 2 gives for the ratio of photoionisation rates $\Gamma_{\rm H\,I}/\Gamma_{\rm He\,II} = 2^{2\alpha+2}$. Combining this result with Eq. 1 and $\alpha_{\rm He\,III} \simeq 5.3\alpha_{\rm H\,II}$ gives $f_{\rm He\,II}/f_{\rm H\,I} \simeq 5.3 \times 2^{2\alpha+2}$. For PL20, $\alpha = 0.5$ and $< f_{\rm He\,II}/f_{\rm H\,I} > = 38$ with a spread of $\sigma = 11$. The derived relation predicts $f_{\rm He\,II}/f_{\rm H\,I} \simeq 42$, an excellent agreement.

Harder spectra (smaller values for α) reduce $f_{\text{HeII}}/f_{\text{HI}}$. In Fig. 11, the diagonal lines to the right of the leftmost line, which is the most populous in the PL20, MQ20, and HY20 models, correspond to lines of sight that are partially shadowed by dense knots of gas. The spectrum is hardened by the preferential absorption of photons around $\nu_{\rm H\,I}$, shifting the gas in the shadowed region to the right. As the Ifront moves through the dense knot, the spectrum in the shadowed region softens so the diagonal drifts leftward until it coincides with the leftmost diagonal. Similarly, assuming the dominant ionisation states of helium are HeII and HeIII, softer spectra will produce larger ratios, shifting the principal line to the left in Fig. 11. For MQ20 and HY20, $\langle f_{\rm He\,II}/f_{\rm H\,I}\rangle = 46$ and 39 respectively. The starburst spectrum is so soft that $\langle f_{\text{He II}}/f_{\text{H I}} \rangle$ is essentially infinite. Otherwise, the linear correlation expected is indeed found.

In the presence of a hard spectrum, $f_{\rm He\,II}$ is dependent on the gas density, with greater densities leading to less He II destruction. The dependence of the destruction on density is illustrated in Fig. 11 where the colour is correlated with gas density. In the case of the soft star-burst spectrum, He II creation does not occur until hydrogen ionisation is well under way ($f_{\rm H\,I} < 0.05$).

Parametrized by the gas density, $f_{\rm H\,I} = \alpha (\rho/\bar{\rho})^{\beta}$ where $\alpha = 2.387 \pm 0.001 \times 10^{-4}$, $1.782 \pm 0.001 \times 10^{-4}$, $2.107 \pm 0.002 \times 10^{-4}$ and $\beta = 0.6401 \pm 0.0007$, 0.6227 ± 0.0006 , 0.838 ± 0.001 for PL20, MQ20, and HY20 respectively. Similarly, $f_{\rm He\,II} = \alpha (\rho/\bar{\rho})^{\beta}$ where $\alpha = 1.038 \pm 0.006 \times 10^{-2}$, $9.129 \pm 0.006 \times 10^{-3}$, $9.316 \pm 0.008 \times 10^{-3}$ and $\beta = 0.6620 \pm 0.0007$, 0.6517 ± 0.0006 , 0.860 ± 0.001 for PL20, MQ20, and HY20 respectively. Cosmic variance leads to errors in α of about 10 per cent and β of about 2 per cent.

The power law dependence of ionisation fraction on density is expected if the shape of the local ionising spectrum is constant and the density and temperature are related through a power law, though the exponent deviates from a simple adiabatic relation. The equilibrium rate equation for hydrogen is $n_{\rm H\,I}\Gamma_{\rm H\,I}=n_en_{\rm H\,II}\alpha_{\rm H\,II}$. Assuming almost complete ionisation, the ionisation fraction is,

$$f_{\rm H\,I} \simeq \frac{n_e \alpha_{\rm H\,II}}{\Gamma_{\rm H\,I}}.$$
 (4)

We recall that the photoionisation rate, $\Gamma_{\rm H\,I}$, is a function of the shape of the local ionising spectrum. Assuming it is constant and that ionisation is almost complete, the neutral fraction follows, $f_{\rm H\,I} \propto \rho \alpha_{\rm H\,II}$. Over the temperature range of interest, the recombination rate responds to the temperature as $\alpha_{\rm H\,II} \propto T^{-0.69}$. If the density and temperature are related polytropically, $T \propto \rho^{\gamma-1}$, then $f_{\rm H\,I} \propto \rho^{1-0.69(\gamma-1)}$. From our power law fits above, the inferred values for γ are 1.522 ± 0.001 , 1.5468 ± 0.0009 , and 1.235 ± 0.001 for PL20, MQ20, and HY20 respectively. For He II the inferred values are $\gamma = 1.490 \pm 0.001$, 1.5048 ± 0.0009 , and 1.203 ± 0.001 PL20, MQ20, and HY20 respectively. Except for the HY20 model, the values of γ are comparable to those found by directly fitting the $\rho-T$ relation in Sec. 3.1. The difference for HY20 (1.235 \pm 0.001 versus 1.13 ± 0.01) may simply be a result of the broad $\rho-T$ distribution.

The shallow $\rho-T$ profile from the hybrid model is explained by the memory of the recent HeII reionisation retained in the low-density gas (Meiksin 1994). The shallow profile is due to hotter low-density gas, not cooler high-

density gas (Fig. 9, lower-right panel). Indeed, all the gas is hotter, the low-density gas more so. The radiation field at z=3 is the same as that produced by the pure power-law spectrum. What differs is that the helium was ionised more recently in the hybrid model than in the other models. The lack of dependence on $z_{\rm on}$ is due to the time difference between $z_{\rm on}$ (20, 12, or 8) and z=3 being greater than a critical amount. For the hybrid model, $z_{\rm trans}=5$. Returning to Figures 7 and 8, it is noteworthy that the temperature distributions for $z_{\rm on}=8$ are marginally hotter for all the models except the hybrid, for which they are all identical. There is a critical redshift $z_{\rm on}\lesssim 8$ for which the independence of the gas temperature from the reionisation epoch is lost, and it is the low density gas that is most susceptible.

For the hard spectra, the colour scale of Fig. 11 indicates that higher gas densities correlate with higher $f_{\text{He II}}$ at a constant $f_{\rm H\,I}$. A much weaker trend is found by Maselli & Ferrara (2005) for overdensities smaller than 10. Because $N_{\rm HI}$ increases with gas density, the trend found here may manifest itself in the data as an increase in $\eta = N_{\rm HeII}/N_{\rm HI}$ with $N_{\rm HI}$. A firm prediction, however, must rely on spectral fits of the absorption features. This is deferred to a later paper. But a few comments on η are made here. First, since $\eta = (n_{\rm He}/n_{\rm H})(f_{\rm HeII}/f_{\rm HI})$, where $n_{\rm He}/n_{\rm H} \approx 1/13$ is the number ratio of helium to hydrogen atoms, the values for η found in the simulation lie well below the median measured value of about 50 (Zheng et al. 2004). This indicates that the ionising spectrum should be much softer than in our model. This may in part be due to the known underprediction in the number of Lyman Limit systems (Gardner et al. 1997; Meiksin & White 2004), which significantly filter, and soften, the spectrum as the ionisation field filters through the IGM (Madau & Meiksin 1994; Haardt & Madau 1996). But it may also be a consequence of our chosen input spectra. Choosing $\alpha = 2$ instead of 0.5 for the power law spectrum would increase η by a factor of 8 for the power-law model even without the filtering effect of the IGM. Boosting the ratio of the contribution of the galaxy to the QSO spectrum in the hybrid model would achieve a similar effect.

Large fluctuations are found in the ratio $f_{\rm HeII}/f_{\rm HI}$, which directly translate into the same fluctuations in η . A change in the softness of the radiation field would leave the fluctuations in η largely unaffected. The ratio varies by a little under 2 dex, resulting both from the inhomogeneities in the radiation field and a wide spread in gas temperatures due to radiative transfer, particularly in the low density gas which gives rise to most of the HeII features. This spread, however, is smaller than found by Zheng et al. (2004), who report a spread of at least 2.5 dex in η at $z \lesssim 3$. Particularly in contrast to our findings are several systems with lower limits of $\eta > 1000$.

Our findings also disagree with the discovery of Reimers et al. (2005) of several voids, as revealed by low H_I optical depths, for which the He_{II} optical depths are very high. This supports the conclusion of Reimers et al. (2005) that the voids may be blocked by dense structures absorbing the He_{II} ionising radiation. Some such regions are shown in Fig. 12. The presence of a dense knot in a filament may cast a long shadow in He_{II} ionising photons traversing voids as well as filaments. The simulations, however, do not appear to produce as high a frequency of such systems as found by Reimers et al. (2005). Our simulations are restricted in

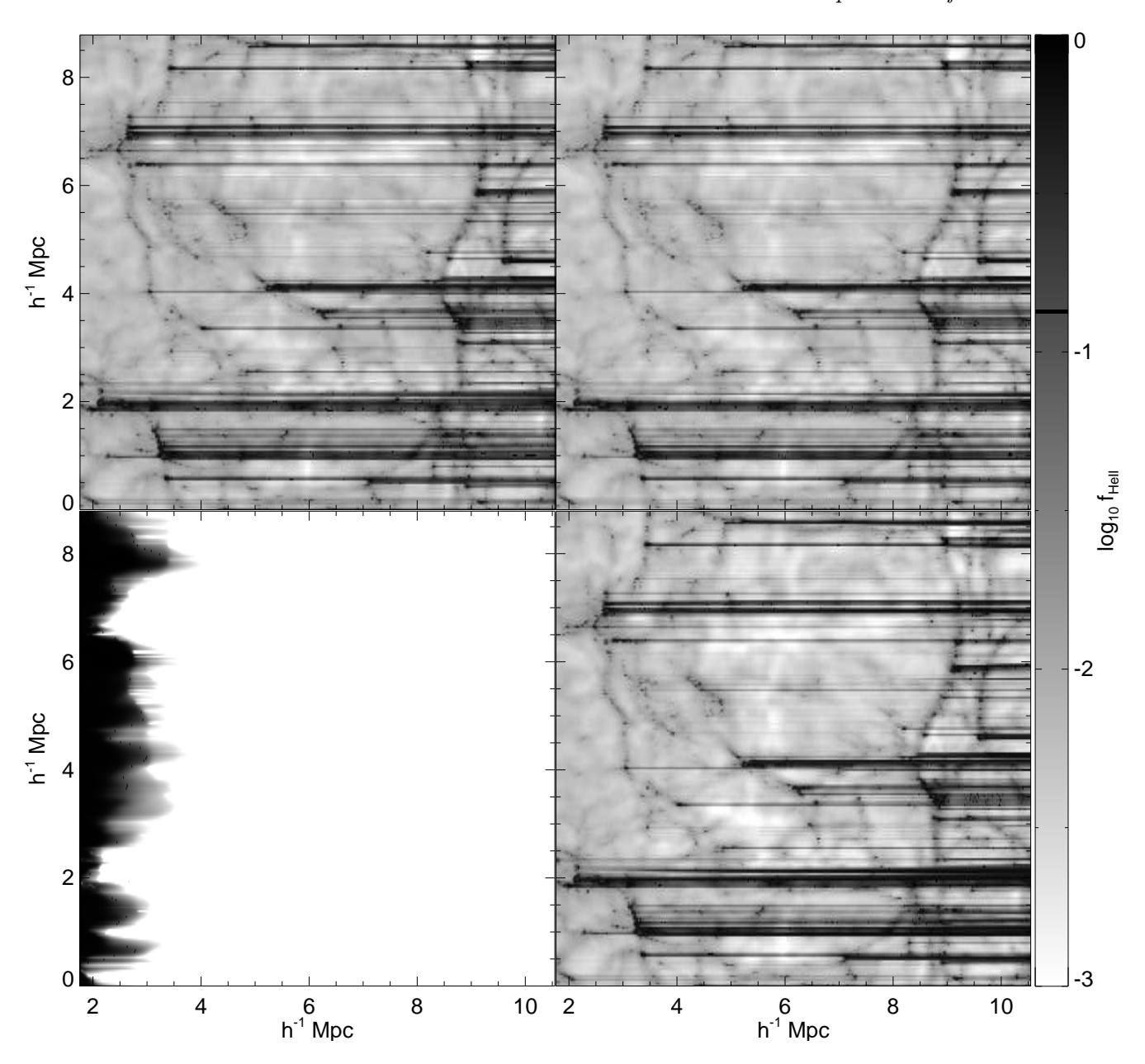


Figure 12. The He II fraction at z=3. From top-left to bottom-right the panels correspond to PL20, MQ20, SB20, and HY20.

that they only include the passage of an I-front from a single direction, while after reionisation is largely completed, many I-fronts will have overlapped. Nonetheless, pockets of high He II may persist for long times if shielded by dense knots from QSOs sufficiently close to otherwise ionise the gas. Allowing for such shielding, along with additional Lyman Limit systems, may help to reconcile our findings with the very high η systems found by Zheng et al. (2004) and Reimers et al. (2005). Shielding increases the spread in η in simulations without radiative transfer effects (Bolton et al. 2006). It is possible that shielding combined with an inhomogeneous field and the variations in ionisation rates and temperature (which affects the recombination rates) found here may successfully account for the measured fluctuations. It may not be possible to account for the most extreme sys-

tems ($\eta > 1000$) without local sources of H I ionising photons too soft to ionise He II.

For the starburst model (lower-left frame of Fig. 11) the hydrogen is ionised before the helium and the helium never reaches the He III state. Hence the history proceeds from the lower right to the lower middle then to the upper middle. Helium ionisation is limited to domains in which $f_{\rm HI} \lesssim 10^{-3}$ but can be any value, independent of $f_{\rm HI}$ and density.

The role played by helium in heating the gas is illustrated in Fig. 13 for the power-law model (PL08). A boost in temperature by about 20 per cent is produced by helium ionisation compared with hydrogen ionisation alone.

The even higher temperatures produced by the hybrid model are directly attributable to the presence of helium. Recall that between z=5 and 4, the irradiating spectrum undergoes a transition from a starburst to a power-law spec-

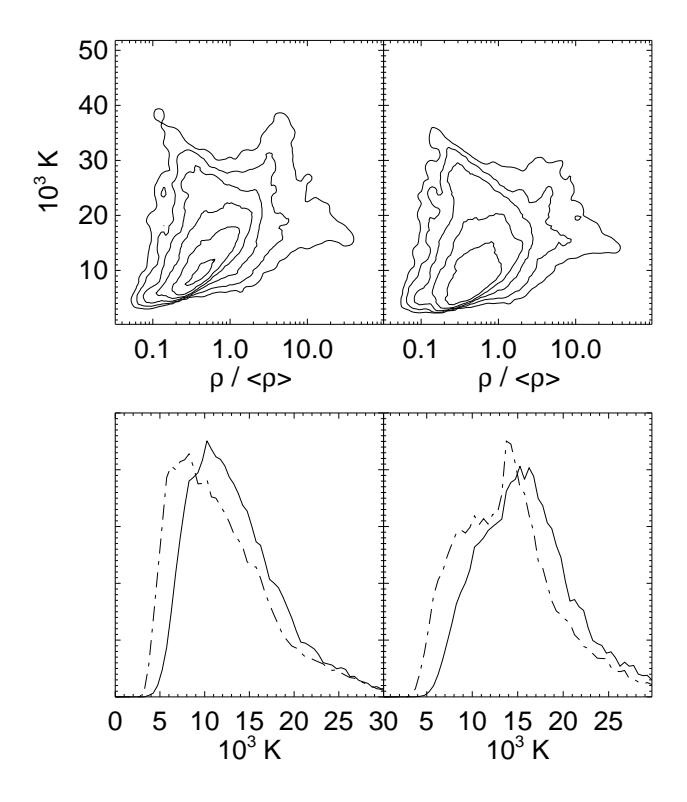


Figure 13. Comparison of thermal state of gas with and without helium ionisation. The top panels illustrate the $\rho-T$ distribution with (left) and without (right) helium ionisation. The lower panels show the modification to the volume-weighted (left) and mass-weighted (right) temperature distributions produced with (solid) and without (dot-dashed) helium ionisation.

trum. As a consequence of the soft spectrum ionising prior to the hard, the hydrogen I-front precedes the helium Ifront. Since ionised gas cannot be heated significantly by a radiation field, no matter how hard the spectrum, without helium the harder power-law spectrum has no effect on the gas previously ionised by the starburst spectrum. Gas that has not yet been ionised is heated to higher temperatures than that ionised by the starburst spectrum since more energy, $h(\nu-\nu_0)$, is liberated per ionisation. In Fig. 14, bottom panel, the differential heating in a hybrid model without helium is illustrated. The gas ionised prior to the transition to the power-law spectrum remains unaffected by the transition. The gas previously unionised is ionised and heated to higher temperatures. With helium (top panel of Fig. 14) the transition of the spectrum heats all the gas along the line of sight. This is not surprising since ionisation of helium leads to heating. What is notable is that the gas is heated more than if the power-law spectrum ionised a completely neutral medium.

A HeII I-front passing through HII-dominated gas leads to a larger jump in temperature than a HI front passing through HeIII-dominated gas. (Note that in both cases, the final state is fully ionised.) The temperature-entropy relation $T = \mu(m_{\rm H}/k)S\rho^{\gamma_{\rm ad}-1}$ explains the differential temperature jumps. The mean molecular weight is given by $\mu m_{\rm H}$ where $m_{\rm H}$ is the mass of a hydrogen atom, S is the entropy, and k is the Boltzmann constant. In the case of the HeII-HeIII transition in a HII-dominated gas, μ is reduced by only 7 per

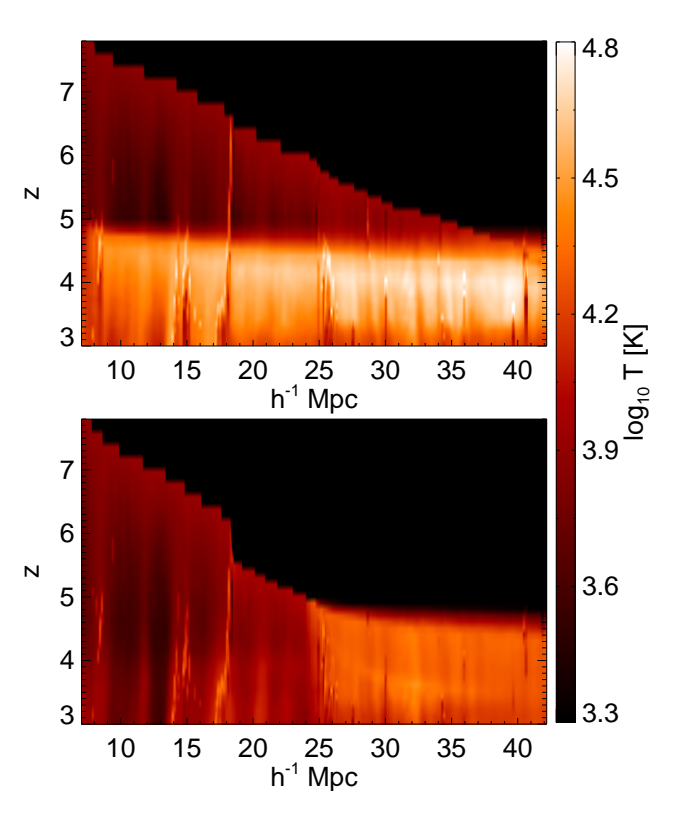


Figure 14. The importance of helium in the hybrid model. Illustrated is the evolution of the temperature of a single line of sight in a HY08 simulation with (top) and without (bottom) helium. The transition between starburst and power-law spectrum occurs between z=5 and 4.

cent, leaving any gain in entropy to translate into a gain in temperature. In the alternate case of the H_I-H_{II} transition in a gas where He_{III} is the dominate helium species, μ drops by 45 per cent, almost halving the gain in entropy. There is still a net gain in temperature, but it is only about 10 per cent.

3.4 Clumping

It has long been recognized that clumping of gas may substantially slow the propagation of I-fronts due to the increased rate of radiative recombinations (Shapiro & Giroux 1987; Meiksin & Madau 1993; Madau & Meiksin 1994). Estimates of the importance of clumping have varied, but recently tend toward only a moderate slowdown of the I-fronts (Sokasian et al. 2003; Meiksin 2005; Ciardi et al. 2006).

We have estimated the role clumping may play in delaying reionisation by comparing the growth of the H $\scriptstyle\rm II$ filling factor in the simulations with that predicted for a uniform IGM. While the results, illustrated in Fig. 15, show a moderate delay in the growth of the filling factor, particularly at high redshifts, we do not find a strong effect. It is possible the effect is underestimated because of the deficit of small dense structures like Lyman Limit systems found in N-body simulations. A definitive result may need to await hydrodynamical computations that reproduce the statistics of Lyman Limit systems and denser intergalactic structures.

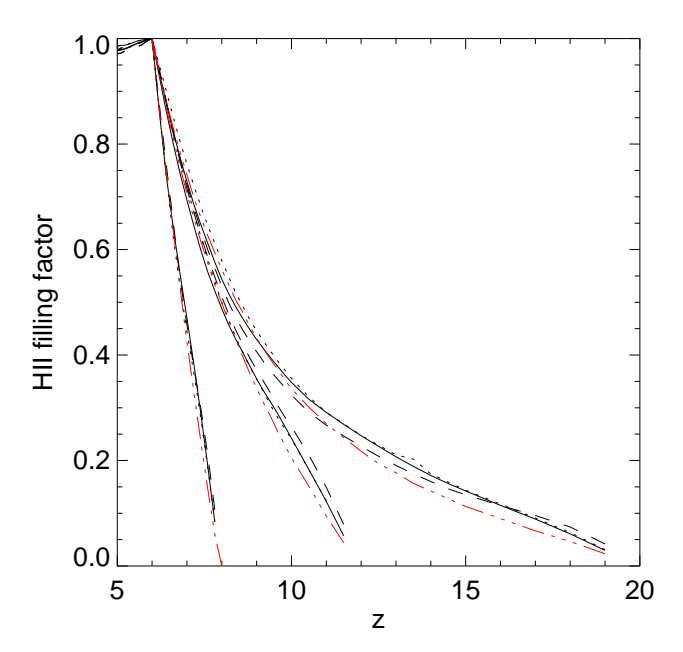


Figure 15. Relative ionisation rates and sensitivity to clumping. The fraction of the total volume in which hydrogen is ionised by z=6 is plotted for the models: power law (solid), mini-quasar short (dashed), and starburst (long-dashed) for $z_{\rm on}=20,12$, and 8. The hybrid model follows the same history as the starburst model prior to z=6. A simple model in which a uniform density gas $(\rho=\Omega_g\rho_c(1+z)^3)$ is ionised by constant flux of ionising photons is plotted as the dash-dot-dot-dot line. Again, there are three separate redshifts at which the source turns on. It should be noted that this figure gives no indication of the absolute rate at which the gas is ionised.

4 DISCUSSION

We have coupled a radiative transfer code based on a probabilistic photon transmission algorithm to a Particle-Mesh N-body code in order to study the sensitivity of the postreionisation temperature of the Intergalactic Medium on source spectrum and epoch of reionisation. We performed multiple simulations with different spectra of ionising radiation: a power law ($\propto \nu^{-0.5}$), miniquasar, starburst, and a time-varying spectrum that evolves from a starburst spectrum to a power law. The power law and miniguasar spectra produced almost identical temperature distributions, owing to their similar shapes. A wider spread of temperatures is found for the remaining models. The mass-weighted mean gas temperatures at z=3 are 6600 K, 17000 K, and 20000 K for the starburst, power law, and hybrid model respectively. A fit to the polytropic relation, $T = T_0(\rho/\bar{\rho})^{\gamma-1}$, gives $T_0 = 15000 \pm 200, 14800 \pm 200, 3700 \pm 50, 19300 \pm 200$ and $\gamma = 1.52 \pm 0.01$, 1.53 ± 0.01 , 1.54 ± 0.01 , 1.13 ± 0.01 for the power-law, mini-quasar, starburst and hybrid models, respectively, at z=3. The errors are formal fit errors. The values are nearly independent of the epoch of H_I reionisation. Turning the source on alternately at a redshift of 20, 12, and 8 made little change to the temperature of the IGM at z = 3. Independence of $z_{\rm on}$ is beneficial to using temperature as a source discriminator: there is no $z_{\rm on}$ -source

The He II I-front passing through H II-dominated gas leads to a larger jump in temperature than the H I I-front

passing through HeIII-dominated gas. Indeed, it is seen in the simulations with the power law spectrum that the temperature increase is only about 10 per cent when a trailing H_I I-front passes through gas in which helium is fully ionised. Implied is that a significant temperature change will not be produced around a hard source by the passage of a H_I I-front, in contrast to a soft source or a region in which hydrogen was fully ionised prior to helium.

The post-ionisation temperature of the IGM may be used as a key observable for identifying the source of reionisation. While moderate to high overdensity gas establishes an equilibrium temperature in which photoionisation heating balances atomic radiative cooling processes, the equilibrium time scale exceeds a Hubble time in lower density regions, those that give rise to optically thin Ly α absorption systems. In contrast to optically thin models, we find a broad fanning out of the temperature-density relation for underdense regions with temperatures exceeding 3×10^4 K achieved. This may help substantially in reconciling the much larger Doppler parameters measured, with a median value of about $30 \,\mathrm{km}\,\mathrm{s}^{-1}$, for the optically thin Ly α systems at $z \approx 3$ than predicted by simulations without radiative transfer (Meiksin et al. 2001). Even allowing for bulk motions to contribute as much as half to the line widths (in quadrature) requires a gas temperature of 2.8×10^4 K. The hybrid model, with late Heureionisation, comes closest to meeting this requirement.

Hardening of the spectrum due to passage through structures with high H_I column densities leads to fluctuations in the $f_{\rm He\,II}/f_{\rm H\,I}$ ratio in the shadowed regions. A harder spectrum decreases the ratio. Consequently, if only one source (or sources with similar spectra) is contributing to the metagalactic intensity, fluctuations in the $f_{\rm He\,II}/f_{\rm H\,I}$ ratio should tail toward lower values. A spread is indeed found in the data (Zheng et al. 2004; Reimers et al. 2005). The spread, however, appears to exceed that found in the simulations. In particular, very high He II to H I column density ratios exceeding 1000 found in the data are not recovered by the simulations. It may be that local sources are required to reproduce these extreme values.

ACKNOWLEDGEMENTS

Some of the computations reported here were performed using the UK Astrophysical Fluids Facility (UKAFF). Tittley is supported by a PPARC Rolling-Grant.

REFERENCES

Abel T., Norman M. L., Madau P., 1999, ApJ, 523, 66 Becker R. H., et al 2001, AJ, 122, 2850

Bolton J., Meiksin A., White M., 2004, MNRAS, 348, L43
 Bolton J. S., Haehnelt M. G., Viel M., Carswell R. F., 2006, MNRAS, 366, 1378

Ciardi B., Scannapieco E., Stoehr F., Ferrara A., Iliev I. T., Shapiro P. R., 2006, MNRAS, 366, 689

Ciardi B., Stoehr F., White S. D. M., 2003, MNRAS, 343, 1101

Fernández-Soto A., Lanzetta K. M., Chen H.-W., 2003, MNRAS, 342, 1215

Fioc M., Rocca-Volmerange B., 1997, A&Ap, 326, 950

Gardner J. P., Katz N., Hernquist L., Weinberg D. H., 1997, ApJ, 484, 31

Gnedin N. Y., Abel T., 2001, New Astronomy, 6, 437

Haardt F., Madau P., 1996, ApJ, 461, 20

Madau P., Meiksin A., 1994, ApJ, 433, L53

Madau P., Rees M. J., Volonteri M., Haardt F., Oh S. P., 2004, ApJ, 604, 484

Malkan M., Webb W., Konopacky Q., 2003, ApJ, 598, 878

Maselli A., Ferrara A., 2005, MNRAS, 364, 1429

Meiksin A., 1994, ApJ, 431, 109

Meiksin A., 2005, MNRAS, 356, 596

Meiksin A., Bryan G., Machacek M., 2001, MNRAS, 327,

Meiksin A., Madau P., 1993, ApJ, 412, 34

Meiksin A., White M., 2003, MNRAS, 342, 1205

Meiksin A., White M., 2004, MNRAS, 350, 1107

Meiksin A., White M., Peacock J. A., 1999, MNRAS, 304,

Miralda-Escude J., Rees M. J., 1994, MNRAS, 266, 343 Nakamoto T., Umemura M., Susa H., 2001, MNRAS, 321,

Osterbrock D. E., 1989, Astrophysics of Gaseous Nebulae and Active Galactic Nuclei. University Science Books, Sausalito, CA

Razoumov A. O., Norman M. L., Abel T., Scott D., 2002, ApJ, 572, 695

Reimers D., Fechner C., Hagen H.-J., Jakobsen P., Tytler D., Kirkman D., 2005, A&Ap, 442, 63

Schaye J., Theuns T., Rauch M., Efstathiou G., Sargent W. L. W., 2000, MNRAS, 318, 817

Shapiro P. R., Giroux M. L., 1987, ApJ, 321, L107

Sokasian A., Abel T., Hernquist L., Springel V., 2003, MN-RAS, 344, 607

Spergel D. N., et al 2006, ArXiv Astrophysics e-prints, arXiv:astro-ph/0603449

Spergel D. N., Verde L., Peiris H. V., Komatsu E., Nolta M. R., Bennett C. L., Halpern M., Hinshaw G., Jarosik N., Kogut A., Limon M., Meyer S. S., Page L., Tucker G. S., Weiland J. L., Wollack E., Wright E. L., 2003, ApJS, 148, 175

Whalen D., Norman M. L., 2006, ApJS, 162, 281

Zhang Y., Meiksin A., Anninos P., Norman M. L., 1998, ApJ, 495, 63

Zheng W., Kriss G. A., Deharveng J.-M., Dixon W. V., Kruk J. W., Shull J. M., Giroux M. L., Morton D. C., Williger G. M., Friedman S. D., Moos H. W., 2004, ApJ, 605, 631